Room Temperature, Air Crystallized Perovskite Nanorods for High Performance Solar Cells

Ashish Dubey[1], Nick Kantack[1], Nirmal Adhikari[1], Swaminathan Venkatesan[1], Mukesh Kumar[2], Khan Mamun Reza [1], Devendra Khatiwada[1], Seth B. Darling[3,4], Qiquan Qiao[1*]

[1]Center for Advanced Photovoltaics, Electrical Engineering and Computer Science Department, South Dakota State University, Brookings, SD 57007, USA

[2]Functional and Renewable Energy Materials Laboratory, Department of Physics, Indian Institute of Technology Ropar, Punjab 140 001, India

[3]Center for Nanoscale Materials, Argonne National Laboratory, 9700 S. Cass Avenue, Argonne, IL 60439

[4]Institute for Molecular Engineering, University of Chicago, 5640 S Ellis Ave, Chicago, IL 60637

Abstract

For the first time, room temperature growth and crystallization of perovskite nanorod films in ambient air without use of thermal annealing was reported. Highly efficient perovskite nanorod-based solar cells were made using ITO/PEDOT:PSS/$CH_3NH_3PbI_3$ nanorods/$PC_{60}BM$/Rhodamine/Ag. All the layers except PEDOT:PSS were processed at room temperature thereby eliminating the need for thermal treatment. Perovskite films were spin coated inside a N_2 filled glove box and immediately were taken outside in air having 40% relative humidity (RH). Exposure to humid air was observed to promote the crystallization process in perovskite nanorod films even at room temperature. Perovskite nanorod films kept for 5 hours in ambient air showed nanorod-like morphology having high crystallinity, with devices exhibiting a PCE of 14.27%, which is much higher than the PCE of 11.31% for traditional thermal-annealed perovskite film based devices. It was concluded that moisture plays an important role in room temperature crystallization of pure perovskite nanorods, showing improved optical and charge transport properties, which resulted in high performance solar cells.

Keywords: Room temperature, un-annealing, air growth, moisture, perovskite nanorods, crystalline, solar cells

1. Introduction

Perovskite based solar cells have been of great interest because of its high power conversion efficiency compared to previous generation solar cells such as CZTS [1], DSSCs [2, 3, 4, 5, 6], small molecule [7] and polymer solar cells [8, 9, 10, 11, 12, 13, 14, 15, 16, 17, 18, 19, 20, 21, 22, 23]. Methylammonium lead halide ($CH_3NH_3PbI_3$) based organic-inorganic planar perovskite solar cells has seen rapid increase in efficiency with low cost simple solution processing fabrication[24]. Single halide ($CH_3NH_3PbI_3$) perovskite has been widely studied in both planar [25] and mesoporous device structure [26, 27, 28]. With ongoing development in perovskite based solar cells, several perovskite film formation techniques have been reported such as single-step spin coating of a mixed precursor solution [29], single-step spin coating with additives or additional solvents [30, 31, 32], sequential deposition method [33], two-step spin–coating method [34], vapor-assisted solution process approach [35], evaporation of precursor materials [36] and spray-deposition[37]. Most of these different perovskite growth methods have shown device power conversion efficiency (PCE) more than 10%, with one of the methods exhibiting a record efficiency of 20.1% [38]. However among the above methods, one-step deposition of perovskite film in planar architecture is desired because of its low temperature processing, smooth morphology and simplicity in device fabrication.

To further simplify fabrication of one-step deposition of perovskite-based planar devices and improve perovskite film morphology, there is a need for room temperature slow crystallization of pure perovskite phase in ambient atmosphere. This achievement would not only simplify the perovskite crystallization, but also open avenues to realize perovskite films on flexible substrates using low temperature, ambient air processing. Until now, there have been few reports on processing of perovskite film at room temperature and ambient air. A report on a spin coated bilayer of PbI_2/CH_3NH_3I demonstrated the complete conversion to perovskite phase was achieved by keeping the film in ambient air for 60 min followed by thermal annealing, which led to an increase in perovskite crystallinity [39]. Another report on room temperature processing of perovskite was reported where a small amount of NH_4Cl was added to precursor

solution (CH_3NH_3I, PbI_2 in dimethylformamide (DMF)), which was then spin coated at room temperature with perovskite film being crystallized during spinning resulting in a dark brown color perovskite film, which showed a device efficiency of 9.32% [40]. Further room temperature processing of perovskite was also achieved using a solvent-solvent extraction technique, where a spin coated $MAPbI_3$ film was immersed immediately in diethyl ether solvent at room temperature, which in turn, converts the $MAPbI_3$ thin film into perovskite in 2 min [41]. All these room temperature processing of perovskite involve partial annealing of films, addition of extra dopant, or washing in a solvent.

One of the challenges for ambient air processing of organic-inorganic perovskite films is their degradation in due to moisture. Perovskite films are prone to degradation from moisture present in the atmosphere, requiring processing and crystallization in a N_2 filled glove box. The most common procedure followed for crystallization of perovskite films is annealing on top of a hot plate inside inert atmosphere. This method of crystallization of perovskite not only increases the complexity of fabrication, but also makes it difficult to control perovskite film crystallinity and morphology at the nanoscale level. As reported previously, the perovskite phase is formed by inter-diffusion of precursor elements (CH_3NH_3I and PbI_2) whose rate of diffusion controls the rate of perovskite crystallization [34]. Annealing the deposited perovskite film will lead to rapid diffusion of precursors leaving a smaller time window to control the growth of perovskite crystals, thus severely limiting control over film morphology. Improvement in device performance depends largely on the quality of perovskite films [42]; therefore a film with high perovskite phase crystallinity and large pinhole free perovskite crystals is desired for efficient charge transport with reduced recombination. Retarding the rate of crystallization of spin coated perovskite films will assist in slow inter-diffusion of precursor elements leading to improved crystallinity and large, continuous, defect-free perovskite morphology.

To the best of our knowledge, there have been no reports on formation of perovskite nanorods [43] for photovoltaics. In this report we demonstrate room temperature processed perovskite nanorod- based films without the use of post-deposition annealing for solar cell applications. This is the first study on the time-dependent growth and crystallization of perovskite nanorods in ambient air at room temperature. Perovskite nanorod films were slowly crystallized by keeping them at room temperature in ambient air having 40% RH for different

periods of time varying from 0 h, 1 h, 3 h, 5 h, 8 h to 10 h. Perovskite nanorod films crystallized for 5 hours in ambient air showed nanorod morphology having high crystallinity, with devices exhibiting a PCE of 14.27%, which is much higher than the PCE of 11.31% for traditional thermal annealed perovskite film-based devices.

2. Experimental procedures

Materials

Methylammonium iodide (CH_3NH_3I) was purchased from Dyesol. PbI_2 (99%) was obtained from Acros organics. Anhydrous dimethyl sulfoxide (DMSO) (>99.9%) and γ-butyrolactone (>99%) were purchased from Sigma Aldrich. Clevios™ P VP AI 4083 PEDOT:PSS was ordered from Heraeus. $PC_{60}BM$ and Rhodamine was purchased from Nano-C and Sigma Aldrich. All the materials were used as received.

Device fabrication

The planar device structure adopted for fabricating perovskite nanorod solar cells consists of bottom electrode indium tin oxide (ITO), PEDOT:PSS as hole transport layer (HTL), light absorbing perovskite nanorod layer, $PC_{60}BM$ as electron transport layer (ETL), rhodamine as thin interfacial layer and top metal electrode silver (Ag) [44]. Patterned indium tin oxide (ITO) substrates were first cleaned by sonicating the substrates in detergent water, de-ionized water, acetone and isopropyl alcohol for 20 min each. Cleaned ITO substrates were then plasma cleaned in the presence of oxygen for 20 min. PEDOT:PSS was spin coated at 4500 rpm for 90 sec, followed by annealing in air at 135 ºC for 5 min. The samples were then transferred inside a N_2 filled glove box for coating with the perovskite layer. A mixed solution of 581 mg of PbI_2 (1.26 M) and 209 mg of CH_3NH_3I (1.3 M) mixed overnight in 1 ml of γ-butyrolactone : DMSO in 7:3 volume ratio was spin coated at 750 rpm for 20 sec and 4000 rpm for 60 sec, with 160 µl toluene dripped at the middle of total spinning time (40 sec). The films were then crystallized by either thermal annealing (100 ºC, 20 min) or keeping the films in ambient air for different periods of time (1 h, 3 h, 5 h, 8 h, and 10 h). Figure 1 shows the Perovskite nanorod spin coating steps with toluene dripping and its post crystallization in ambient air at room temperature. $PC_{60}BM$ (20 mg/ml in chlorobenzene) was then spin coated on top of the perovskite layer at 2000 rpm for 40

sec and then kept for 15 min inside the glove box for solvent drying at ambient temperature. Rhodamine (0.5 mg/ml in isopropyl alcohol) was then spin coated at 4000 rpm for 40 sec on top of the $PC_{60}BM$ layer. Ag (100 nm) electrode was then deposited using thermal evaporation in high vacuum of 2×10^{-6} mbar. The solar cell active area was 0.16 cm^2, as defined by the shadow mask.

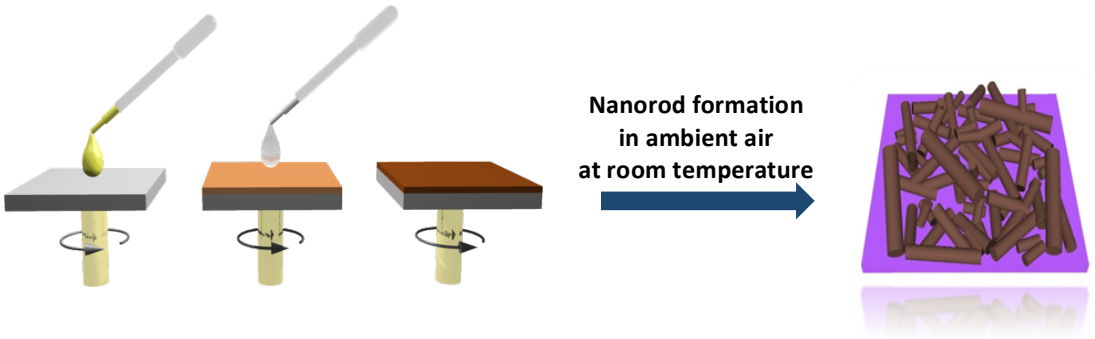

Figure 1. Schematic showing deposition of perovskite nanorod film by spin coating followed by crystallization in ambient air at room temperature.

Characterization

Perovskite nanorod films were characterized for their absorption in the visible and near-infrared regions using an Agilent UV-visible spectrophotometer G1103A. X-ray diffraction (XRD) spectra of perovskite films were recorded with a Rigaku Smartlab diffractometer (2.2 kW Cu-Kα (1.54 Å) radiation). Tapping mode topography and kelvin probe force microscopy (KPFM) images were obtained using an Agilent 5500 scanning probe microscope (SPM) equipped with MAC III controller. The measurements were performed in air having same humidity levels as maintained for the air growth perovskite films. Same Perovskite films at different time intervals were used for measurement where we saw time dependent growth till 5 h and then degradation was seen for longer time. Silicon tips having Cr/Pt coating (Budget Sensors, Multi 75E-G) with resonant frequency of ~75 KHz and force constant of 3 N/m were used for measuring topography and KPFM images. Current density - voltage (J-V) characteristics of perovskite nanorod solar cells were measured in forward (0 - 1 V, 0.01 V interval, 0.01 sec for each interval) and reverse bias (1-0 V, 0.01 V interval, 0.01 sec for each interval) using an Agilent 4155C semiconductor parameter analyzer, keeping perovskite solar cells under illumination (Xenon arc lamp with air mas (AM) 1.5 filter, Newport) with a light

intensity of ~100 mW/cm^2 (AM 1.5). An NREL calibrated photodetector was used to calibrate the distance between Xenon arc lamp and the sample to ensure 100 mW/cm^2 light intensity.

3. Results and Analysis

Figure 2a shows the schematic of the planar device structure with the layer stack ITO/PEDOT:PSS/perovskite nanorods/$PC_{60}BM$/Rhodamine/Ag. In order to determine the light absorption in the solar spectrum, UV-visible absorption spectra of the perovskite nanorod films crystallized in air at room temperature for different periods of time and a control sample that was crystallized by traditional thermal annealing inside N_2 filled glove box were measured. Absorption spectra (figure 2b) of perovskite films at different periods (1, 3, 5, 8, and 10 h) of crystallization in air at room temperature showed increased absorption intensity with respect to increase in perovskite crystallization until 5 h, followed by decrease in absorption intensity beyond 5 h and in the control sample. In the initial hours (1 h and 3 h) of crystallization, the perovskite films showed narrow and lower intensity absorption, which could be attributed to the presence of intermediate phase (MAI-PbI_2-DMSO).[31] At this stage, the film has not been fully crystallized to perovskite phase and consists of a mixed intermediate phase and perovskite phase. As the time of perovskite crystallization in air increases, the absorption intensity increases, indicating time-dependent crystallization of the perovskite phase. Maximum absorption intensity of perovskite nanorod films was obtained for 5 h crystallization in air, showing an optical bandgap ca. 1.5 eV. Perovskite nanorod film crystallized for 8 h in air exhibited an absorption spectrum close to perovskite nanorod film crystallized for 5 h. However, the XRD results show a small PbI_2 peak, and this indicates decomposition of perovskite phase, which will be discussed below. The absorption intensity decreased for perovskite nanorod films crystallized for 10 h in ambient air at room temperature, which could be attributed to further decomposition of single halide perovskite nanorod film from moisture present in air. In order to compare with the control sample, the perovskite film crystallized by thermal annealing in N_2 filled glove box showed lower absorption than 5 h air crystallized film, suggesting improved perovskite nanorod crystallinity in 5 h air growth film. The deposited film was transparent initially and turned to yellowish brown after being kept in ambient air at room temperature for one hour. The film color turned darker when kept for 3 h and was fully darkened at the end of 5 h, suggesting complete crystallization of the perovskite film.

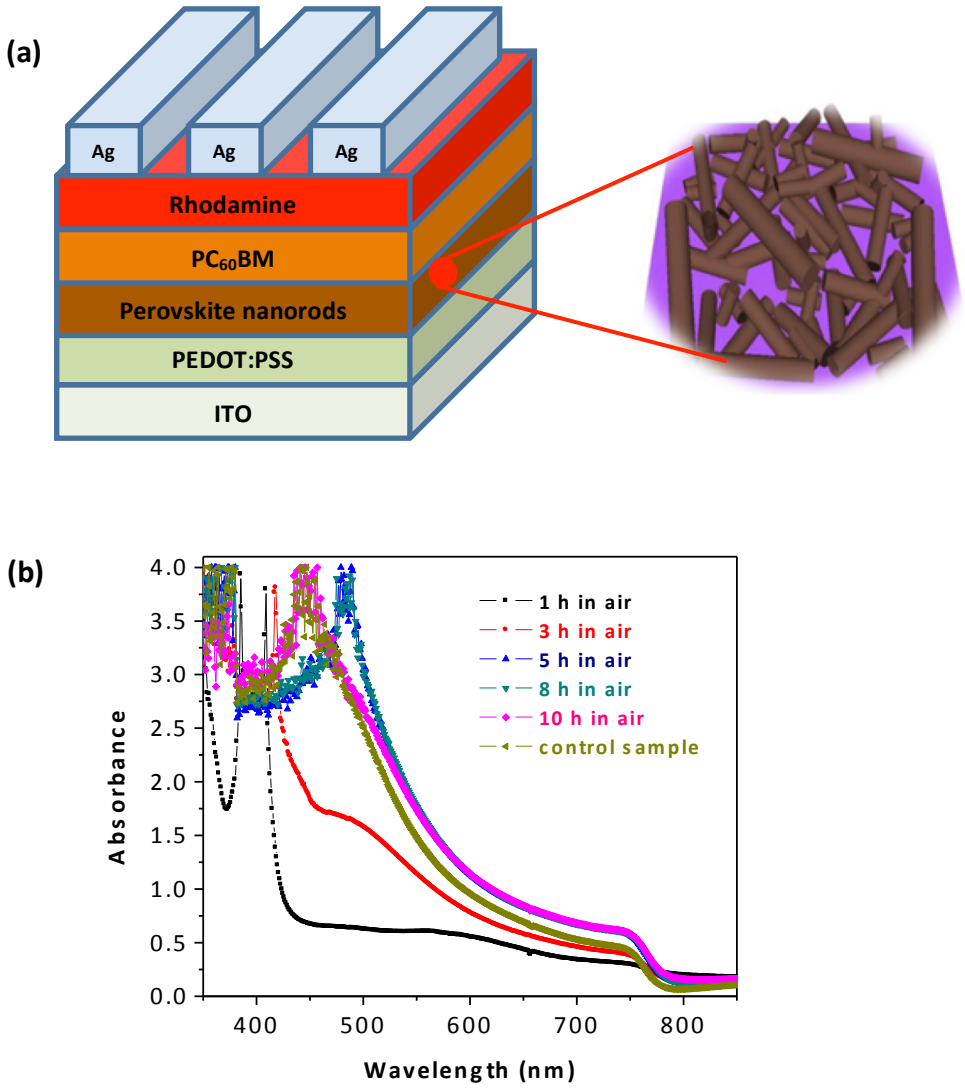

Figure 2. (a) Schematic of perovskite nanorod solar cells; (b) UV-Vis spectra of perovskite nanorod films crystallized in air at room temperature for different time (1, 3, 5, 8 and 10 h) and control sample crystallized by thermal annealing inside N_2 filled glove box.

To understand the growth of perovskite nanorod phase by slow crystallization in air at room temperature, we performed XRD studies. XRD scans (figure 3) were recorded for all the films. Table 1 shows the 2Θ, full width half maximum (FWHM) and peak intensity for (110) and (220) planes of perovskite nanorods. Spin coated films in the initial one hour of air crystallization show weak intensity for the pure perovskite phase peaks occurring at 14º (110) and 28º (220) degrees, but exhibit intense peaks for intermediate phase at 6.5, 7.15 and 9.1

degrees, respectively, suggesting crystalline nature of the intermediate phase in the initial one hour of perovskite crystallization. However, the crystal structure for peaks corresponding to the intermediate phase is still not clearly understood; these peak positions have been observed in previous studies and were related to formation of an intermediate phase, namely MAI-PbI_2-DMSO [31]. As we did not observe any peaks corresponding to PbI_2 phase (~12.6º), we conclude that the deposited perovskite films consist mainly of crystalline intermediate phases (formed by reaction between PbI_2, DMSO and CH_3NH_3I species), which slowly transition to perovskite phase in ambient air by removal of DMSO species at room temperature. The crystallization process of perovskite was further monitored by keeping the perovskite film for 3 h, 5 h, 8 h, and 10 h in ambient air at room temperature. Perovskite films exposed for 3 h show crystallization in air as confirmed by the appearance of intense peaks at 14.1º (110), 28.4º (220) and a small peak at 31.8º (310), with the intermediate phase peaks significantly suppressed, indicating the escape of DMSO from the intermediate phase, which led to increase in perovskite crystallization.

The changes in XRD patterns observed by increasing crystallization time were also reflected in the visual color of film (from light brown at 1 h to further darkening at 3 h and so on). On further keeping the film for 5 h in air, the peaks for intermediate phase at low angle (5-10º) completely disappear, and the intensity of perovskite phase peaks including (110), (220) and (310) increase, suggesting enhancement in the crystalline fraction with increasing air exposure time by complete conversion of crystalline intermediate phase to perovskite nanorods (figure 5c). It was observed from the XRD patterns of 1, 3 and 5 h air crystallized films that the intensity of (110) and (220) and (310) peaks increased significantly in the first 5 h, suggesting orientation of grain growth in all three planes. These perovskite phase peaks correspond to the tetragonal *I*4*cm* crystal structure for highly crystalline single halide perovskite [45, 46]. The (110)/(220) peak intensity ratio increased in the first 5 hours, suggesting preferential grain growth orientation in the (110) plane. Grain growth is determined by their surface and interface energy, which guides the grain growth orientation (lower surface energy planes determines grain orientation) [47]. Since $CH_3NH_3PbI_3$ has tetragonal structure that is less symmetric as compared to its cubic counterpart, there will be a difference in surface energies of different planes, which could be a reason for the higher intensity of the (110) peak. On further exposure of perovskite films in ambient air for 8 h and 10 h duration, a new characteristic peak of PbI_2 at 12.6º appeared with a concomitant decrease in the intensity of major perovskite phase peaks at (110) and (220). This suggests that

once the crystallization to perovskite phase is completed in 5 h, the perovskite film starts decomposing from continued exposure to moisture in air. The appearance of significant PbI_2 peaks in 8 h and 10 h crystallized films also confirms that there is no unreacted PbI_2 until 5 h, and the presence of PbI_2 beyond 5 h air crystallization is attributed to decomposition of perovskite from moisture in air.

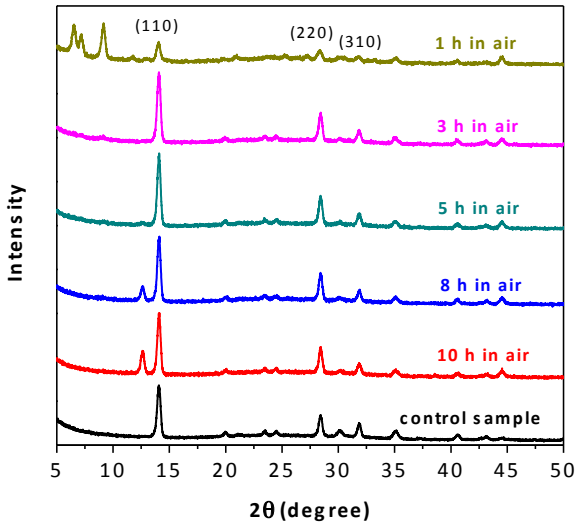

Figure 3. XRD of perovskite nanorod films crystallized in air at room temperature for different time (1, 3, 5, 8 and 10 h) and the control sample crystallized by thermal annealing.

Table 1. 2Θ, full width half maxima **(**FWHM), and intensity in counts for (110) and (220) peaks of perovskite nanorod films crystallized in air for different intervals of time (1, 3, 5, 8 and 10 h) and control sample crystallized by thermal annealing obtained from XRD patterns.

Sample	**2Θ, FWHM, Intensity in counts for (110) peak**	**2Θ, FWHM, Intensity in counts for (220) peak**
1 h in air	14.06, 0.397, 3470	28.31, 0.438, 2505
3 h in air	14.08, 0.362, 9185	28.44, 0.380, 4605
5 h in air	14.10, 0.351, 9445	28.41, 0.344, 4620
8 h in air	14.11, 0.342, 8595	28.42, 0.364, 4460
10 h in air	14.12, 0.348, 8220	28.42, 0.357, 4335
Control sample	14.07, 0.365, 6806	28.41, 0.367, 3443

After carefully investigating the crystallization process of perovskite films in ambient air in comparison with the control sample obtained from thermal annealing in inert atmosphere, one question that still remains to be answered is moisture's role in complete crystallization of single halide perovskite in ambient air. Crystallization of perovskite phase is assisted by interdiffusion of precursor elements in the deposited film. In the case of crystallization by thermal annealing, the solvent species (DMSO) from the intermediate phase is quickly removed, allowing little time for interdiffusion of PbI_2 and CH_3NH_3I, thus restricting the long-range crystalline order in the film, which reduces the overall crystallinity. During slow crystallization of perovskite film in ambient air, our study demonstrates that there is sufficient time for interdiffusion of precursor elements to react and form crystalline perovskite. The slow perovskite crystallization reaction in ambient air is assisted by the presence of airborne moisture, leading to improved crystallinity. The DMSO intermediate phase as observed in our XRD spectrum and also described in the literature [30, 31] was converted to crystalline perovskite phase by thermal annealing at 100 ºC (similar findings were observed in our annealed perovskite film), but in our study we observed that DMSO based intermediate phase conversion happens slowly at room temperature in ambient air. This leads us to the conclusion that moisture in air plays a role in removing DMSO phase at room temperature. Recently, there have been reports on the formation of water-based intermediate phases such as colorless monohydrate ($(CH_3NH_3)PbI_3.H_2O$) and light yellow di-hydrate ($(CH_3NH_3)_4PbI_6.2H_2O$) of $CH_3NH_3PbI_3$ perovskites [39, 46, 48, 49, 50, 51, 52, 53]. It was reported that perovskite forms water-based colorless monohydrate intermediate phase, which crystallizes quickly to crystalline perovskite ($CH_3NH_3PbI_3$) by losing water at room temperature. Apart from monohydrate intermediate formation, it is also well known that DMSO is highly miscible in water. Based on these facts, we hypothesize that DMSO from an intermediate phase (MAI-PbI_2-DMSO) escapes by either solubilizing in water from atmospheric moisture or the water lost from monohydrate intermediate at room temperature. Room temperature crystallization in air involves removal of DMSO-based intermediate phase by solubilization of DMSO in atmospheric moisture. Previous reports showed the PbI_2 exists in form of $[PbI_6]^{4-}$ octahedral layers[31]. CH_3NH_3I and DMSO constituents are intercalated between these octahedral layers forming MAI-PbI_2-DMSO intermediate phase[30, 31]. The DMSO escapes from the intermediate complex by solubilizing in water obtained from atmospheric moisture, leading to immediate crystallization to pure perovskite phase, as shown from schematic in figure 4a. Figure 4b shows

the schematic for the crystallization of perovskite from small elongated features (1 h in air) to large perovskite nanorods at the end of 5 h crystallization in ambient air. This will be confirmed by the AFM measurements discussed below.

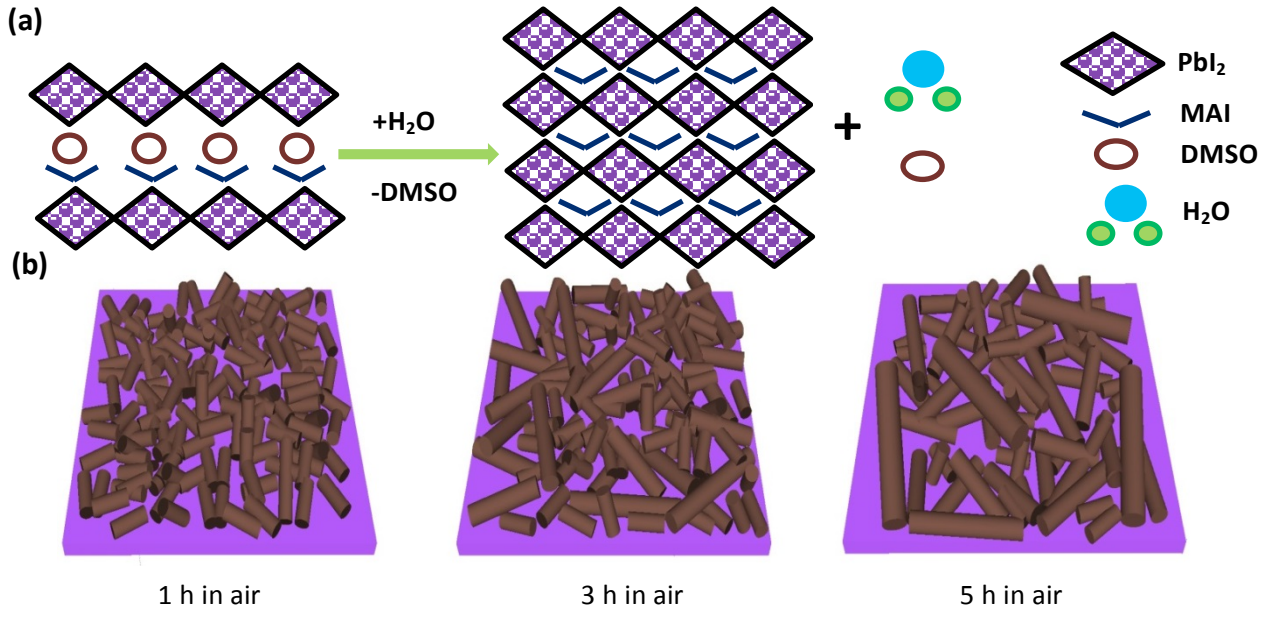

Figure 4. Schematic showing (a) release of DMSO from the layered PbI_2 octahedral structure to crystallize in perovskite nanorod film and (b) change in perovskite nanorod morphology with varying crystallization time in air (1, 3 and 5 h).

In order to determine perovskite interfacial morphology and surface potential of the film, we performed topography and Kelvin probe force microscopy (KPFM) imaging measurements. Figures 5a-f show topography and the corresponding KPFM images in figures 5(g-l) of the perovskite films crystallized by keeping the deposited film for 1, 3, 5, 8 and 10 h in ambient air at room temperature and the control sample crystallized by thermal annealing inside glove box. Topography and KPFM images of the films were recorded simultaneously. As seen from the topography images, the perovskite films in the initial one hour are comprised of dense small grains of perovskite with short elongated features. As time goes on, small features expand into more visible elongated shapes. At 5 h of air exposure, large perovskite nanorod features are formed. The morphological features in 8 and 10 h films are disordered, which could be attributed to decomposition of crystalline perovskite nanorods from moisture in air. This decomposition of pure perovskite nanorod phase crystals is also reflected in XRD peaks (figure 3) of 8 and 10 h

samples, where the intensity of perovskite phase peaks at 14º and 28º is reduced and a small peak at 12.65º appears indicating presence of PbI_2. Root mean square roughness of the films increased for 5 h air crystallized sample (figure 5a) in comparison to 1 h samples (figure 5c). This could be attributed to volume expansion in the 5 h air crystallized film. The 5 h air crystallized films show nanorod shapes with average length of 811 nm and average diameter of 210 nm, whereas thermally annealed films exhibit particle shape with an average particle size of 103 nm. Therefore, the ambient air crystallized films formed nanorods with an aspect ratio of ~3.8. The dimensions of perovskite features were calculated by averaging 20 particles obtained from the topography image (table S1, supplementary information).

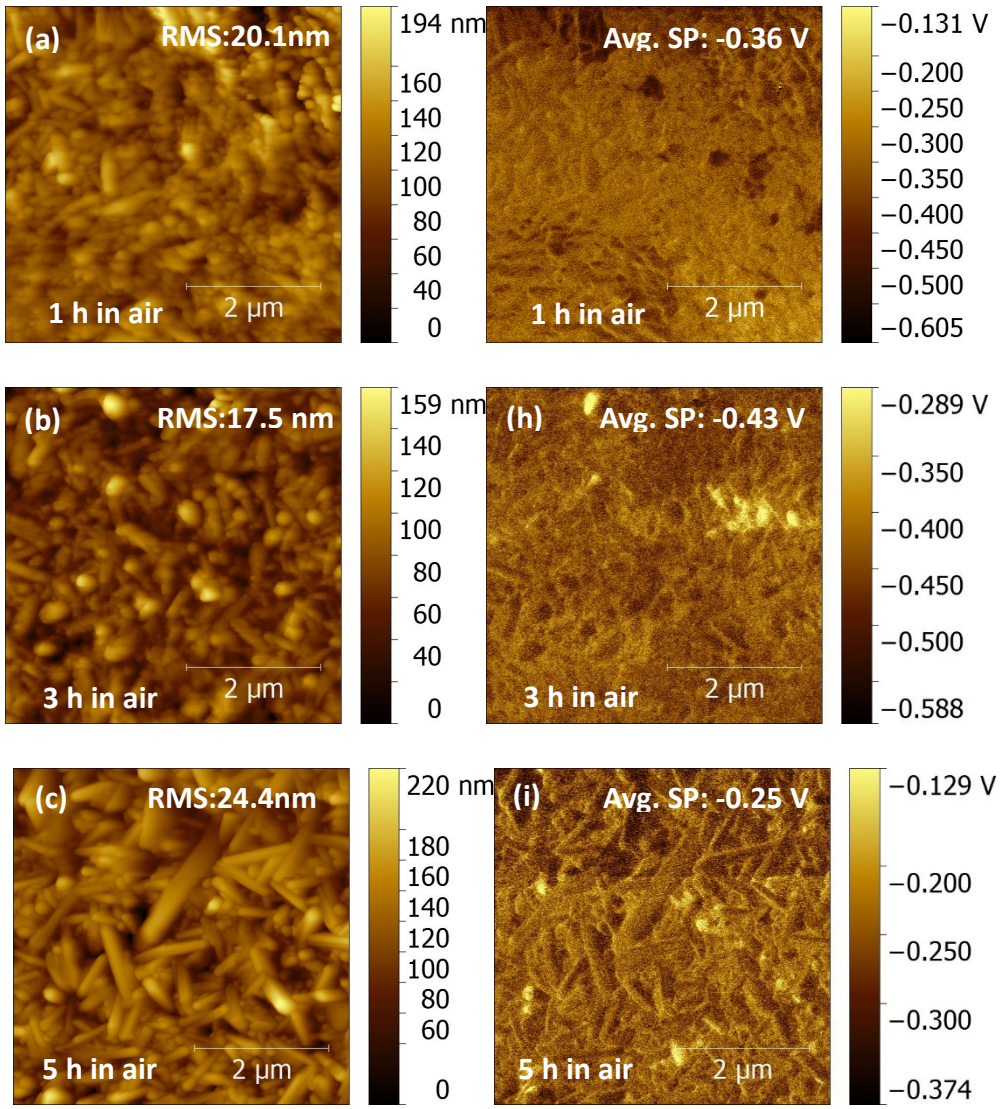

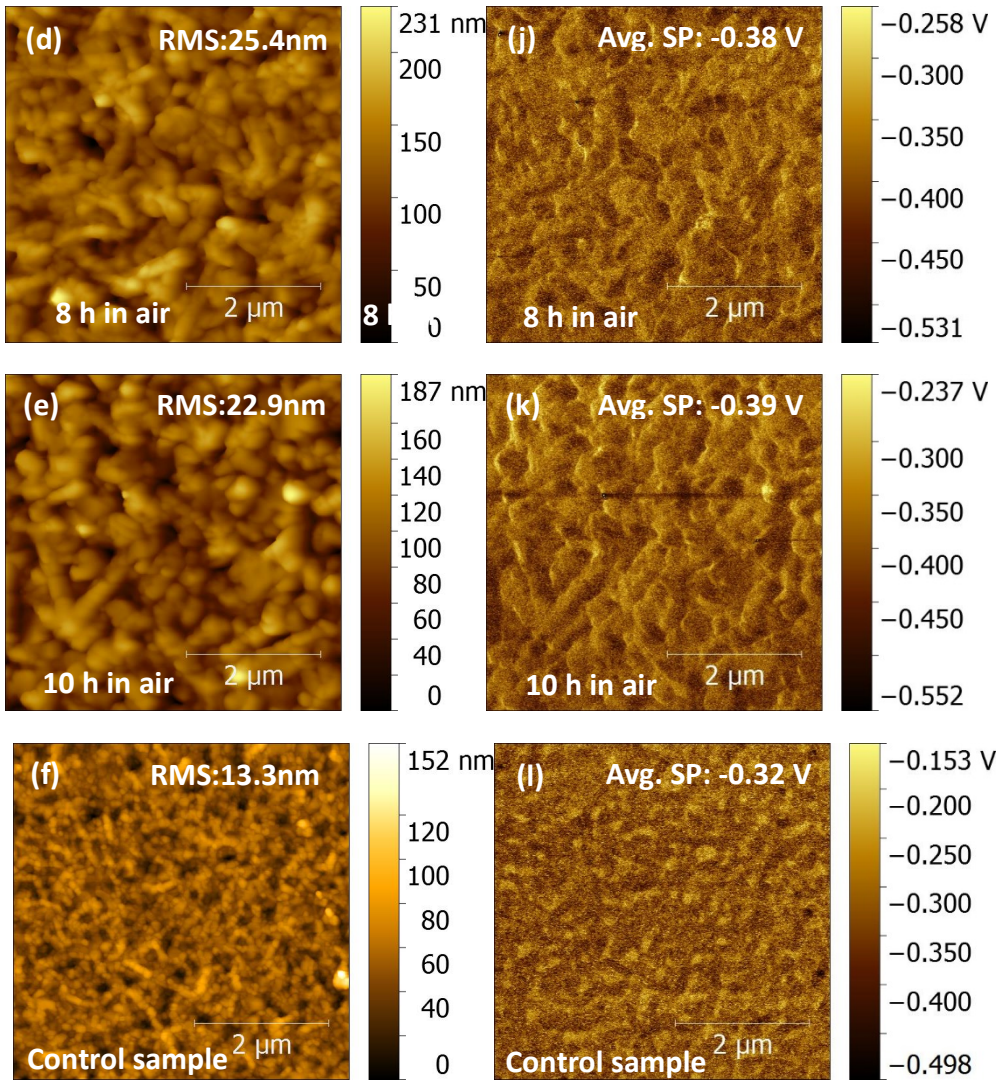

Figure 5. Topography (a-f) and KFM images (g-l) of perovskite nanorod films crystallized in air for 1, 3, 5, 8, 10 h and control sample crystallized by thermal annealing.

KPFM is a method where a conductive tip is used as a kelvin probe to measure surface potential or contact potential difference (CPD) in non-contact mode. The surface potential variation depends on the material phase present in the film. In our study, we investigated the variation in surface potential across the film, which varied for the perovskite intermediate phase, perovskite grain, grain boundaries and for the presence of PbI_2 phase which appears after decomposition of perovskite. During the crystallization process of perovskite and its following decomposition, various material phases appear which will have different surface potential in the

film leading to different magnitude of variation in surface potential across the film. Comparing the KPFM images of air crystallized films at different intervals of time in figure 5(g-k) and the control sample of thermal annealed perovskite film (figure 5l), we observed a change in average surface potential across the surface. In the initial one hour of crystallization in air at room temperature, the film is composed of majority crystalline intermediate phase, a portion of which starts converting to perovskite, showing low average surface potential distribution of -0.36 V. At the end of 3 h, the perovskite sample has a mixed phase of perovskite and intermediate complex, which results in slightly lower average surface potential (-0.43 V) across the film. After 5 h of crystallization in air, the perovskite phase is crystallized, resulting in higher average surface potential of -0.25 V across the film. Beyond 5 h crystallization in air at room temperature, the perovskite phase decomposed and caused new material phase (PbI_2) to appear on the perovskite surface, resulting in a change in surface potential distribution thus having lower average surface potential of -0.38 V after 8 h crystallization. The decrease in average surface potential could be attributed from higher contact potential difference [CPD = $(\Phi_{tip} - \Phi_{sample})/e$], arising from presence of PbI_2 which has low-lying valence band compared to perovskite. At the end of 10 h crystallization in air, even more PbI_2 phase starts appearing as confirmed by XRD spectra (figure 3) causing further slight reduction in average surface potential (-0.39 V) relative to the 8 h film, which could be attributed to increase in mixed phase of PbI_2 and perovskite in the film. On comparison with annealed perovskite film, we found that morphology of annealed perovskite film (figure 5f) consists of small nanoparticle-like features, which is quite different from the nanorod morphology of the 5 h air crystallized film (figure 5c). However, annealed film showed average surface potential of -0.32 V (figure 5l), suggesting nearly same material phase (crystalline perovskite) across the surface, but with smaller grain size and low crystallinity.

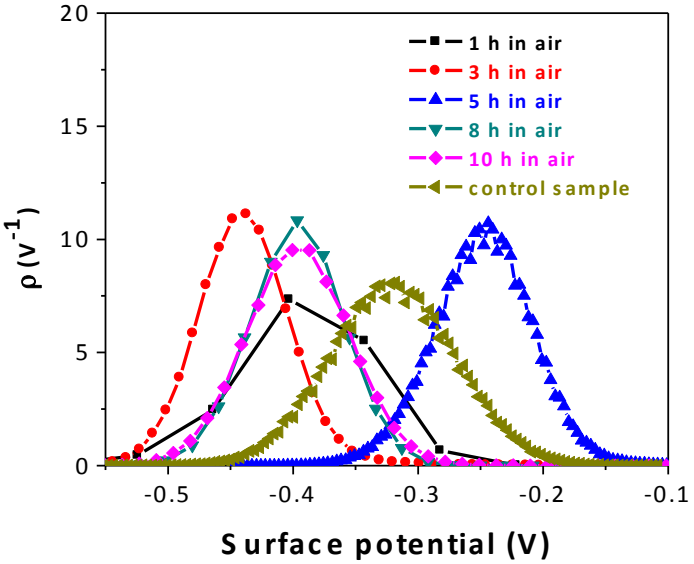

Figure 6. Distribution vs. surface potential curves obtained from KPFM images of perovskite films crystallized in air for 1, 3, 5, 8, 10 h and the control sample made by thermal annealing.

Figure 6 shows distribution vs. surface potential plots for perovskite films crystallized in air for 1, 3, 5, 8, 10 h and control sample films crystallized by thermal annealing in inert atmosphere. All the plots had a qualitatively similar nature of distribution curve, with varying FWHM. A higher average surface potential for 5 h air crystallized film (-0.25 V) compared to thermal annealed control film (-0.32 V) indicates that 5 h air crystallized films have less variation in surface potential across the film suggesting more pure perovskite phase. A higher surface potential for 5 h air crystallized film also indicates reduced defects (trap center for electrons) at perovskite film surface, which mostly occurs as dangling bonds originating due to exposure of iodine atoms in perovskite film.[54] The thermal annealed film showed larger variation in surface potential distribution. Annealing perovskite films at 100 ºC can also lead to decomposition of perovskite by the escape of CH_3NH_3I from the film, which might cause large variation in surface potential across the annealed film. Variation in surface potential distribution could also be attributed to the difference in surface potential at grains and grain boundaries in the films. The 5 h air crystallized films showed large nanorod features suggesting a smaller population of grain boundaries and therefore higher average surface potential (-0.25 V) in

comparison to thermal annealed perovskite film that is comprised of a larger number of grain boundaries causing lower average surface potential (-0.32 V).

All the above performed measurements (e.g., UV-Vis, XRD, topography and KPFM) convey a consistent picture of the morphology evolution. These data support the following mechanism of perovskite crystallization in ambient air at room temperature: immediately after spin coating of precursor solution inside the glove box, the transparent film consists entirely of intermediate phase, which slowly crystallizes into pure crystalline perovskite phase upon exposure in ambient air at room temperature for 5 h. Beyond 5 h, the perovskite film shows irreversible degradation due to moisture where perovskite phase decomposes and PbI_2 phase starts appearing.

Air processed perovskite nanorod films crystallized for different time interval were used for device fabrication, and their performance was compared with annealed perovskite films as control sample devices. J-V curves of all devices and a table of individual device parameters are shown in figure 7a and table 2. All J-V characteristics were recorded at a scan rate of 1 V/s with step of 0.01 V in both forward and reverse directions. Device parameters including short circuit current density (J_{sc}), open circuit voltage (V_{oc}), fill factor (FF) and power conversion efficiency (η%) showed a maximum when room temperature air crystallization time was increased to 5 h with a J_{sc} as 21.63 mA/cm^2, V_{oc} of 0.99, FF of 66.63% and PCE of 14.27%. The devices made from perovskite films aged for 8 and 10 h showed decrease in all device parameters. This decrease is well understood with perovskite film decomposition happening beyond 5 h crystallization in air. Decomposition can decrease light absorption and J_{sc}, increase series resistance with reduced FF, and thus decrease overall PCE. In addition, the control sample devices made from annealed perovskite films showed a PCE of 11.31%, which is lower than the 5 h air crystallized sample. The relatively lower performance could be attributed to reduced crystallization and increased recombination driven by the large number of grain boundaries present in the thermally annealed perovskite film [30, 55]. 5 h air crystallized perovskite nanorods film-based devices showed minimal hysteresis in forward and backward scans as shown in figure 7b, giving an average PCE of 13.95 %. However, a significant hysteresis was observed in annealed perovskite film-based devices, which led to a difference (9.76% forward vs 11.31% reversed) in device efficiency in forward and backward scans. Annealed perovskite films are

comprised of smaller grains with a large number of grain boundaries, which will act as charge recombination centers due to defect and trap states present at grain boundaries and reduce device performance. A histogram showing variation in average efficiency for 10 solar cells is shown in figure 7c for the 5 hour air crystallized perovskite nanorod films (average efficiency at 12.2%) and annealed perovskite films as control sample (average efficiency at 9.2%). Table 2 lists individual device parameters under AM1.5 solar simulator illuminated condition for all sets of devices in both forward and reverse scans.

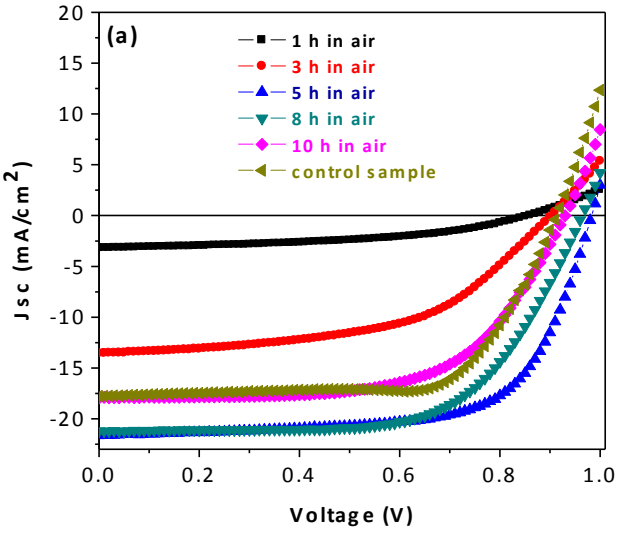

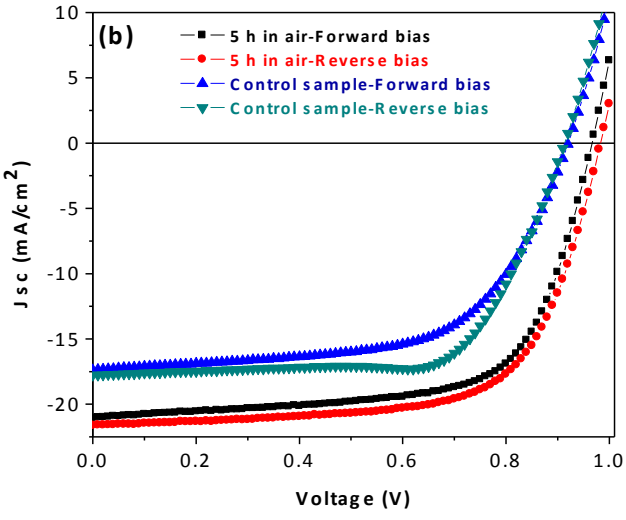

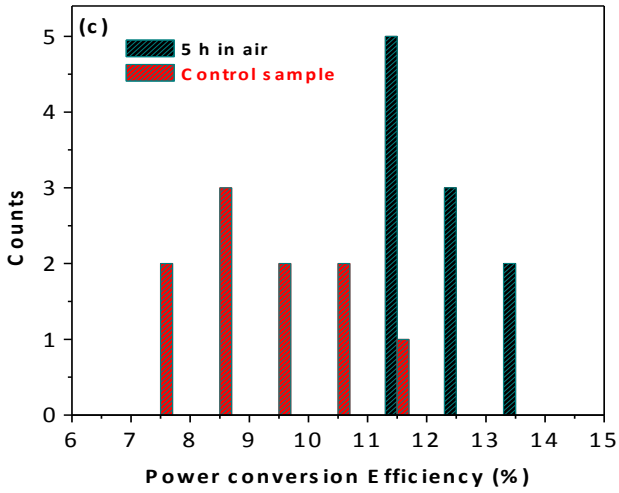

Figure 7. (a) Reverse scan J-V curves for cells made from perovskite films crystallized in air for 1, 3, 5, 8, 10 h and the control sample by annealing, (b) Forward and reverse scan of highest performing device at 5 h air devices and control sample, and (c) Histogram of device efficiencies made from 5 h air crystallized perovskite nanorod films and control samples.

Table 2. Forward and reverse scan photovoltaic parameters for perovskite nanorod solar cells made under different conditions and the control samples.

Sample	Jsc (mA/cm^2)	Voc (V)	FF (%)	PCE (%)	Average PCE (%)
1 h in air-Forward	2.84	0.93	43.85	1.16	1.2
1 h in air-Reverse	3.18	0.86	45.96	1.25	
3 h in air-Forward	13.2	0.96	51.9	6.58	6.52
3 h in air-Reverse	13.58	0.91	52.32	6.46	
5 h in air-Forward	21.05	0.97	66.77	13.63	13.95
5 h in air-Reverse	21.63	0.99	66.63	14.27	
8 h in air-Forward	20.6	0.96	59.8	11.85	12.44
8 h in air-Reverse	21.2	0.97	63.29	13.03	
10 h in air-Forward	16.9	0.94	57.3	9.13	9.71
10 h in air-Reverse	17.9	0.94	61	10.29	
Control sample-Forward	17.3	0.92	61.0	9.76	10.53
Control sample-Reverse	17.7	0.92	69.18	11.31	

Conclusions

In conclusion, we have formed unique crystalline organometal halide perovskite nanorods by crystallizing films completely in ambient air at room temperature. The crystallization processes begins with the formation of DMSO-based intermediate phase that converts to crystalline perovskite nanorod phase in ambient air at room temperature over a period of 5 hours. The growth phase of perovskite nanorod films in ambient air at room temperature and its decomposition were studied in detail using UV-Vis, SPM, and XRD. Morphology evolution from small elongated features to large nanorods was observed by slowly crystallizing the perovskite film in ambient air for up to 5 h. Device performance was measured, revealing 5 hour crystallized perovskite nanorod film with a champion PCE of 14.27%, which is much higher than the champion PCE of 11.31% for traditional thermal annealed perovskite film as control sample. This study of room temperature, ambient air crystallization of perovskite nanorods paves the path for fabrication of low cost and efficient perovskite solar cells on flexible substrates.

Acknowledgement

This research was benefited from the grants including NASA EPSCoR (NNX13AD31A), Pakistan-US Science and Technology Cooperation Program, and NSF MRI (grant no. 1229577 and 1428992). This work was performed, in part, at the Center for Nanoscale Materials, a U.S. Department of Energy Office of Science User Facility under Contract No. DE-AC02-06CH11357.

References:

1. Kumar M, Dubey A, Adhikari N, Venkatesan S, Qiao Q. Strategic review of secondary phases, defects and defect-complexes in kesterite CZTS-Se solar cells. *Energy Environ Sci* 2015, **8**(11)**:** 3134-3159.

2. Sigdel S, Dubey A, Elbohy H, Aboagye A, Galipeau D, Zhang L*, et al.* Dye-sensitized solar cells based on spray-coated carbon nanofiber/TiO2 nanoparticle composite counter electrodes. *Journal of Materials Chemistry A* 2014, **2**(29)**:** 11448-11453.

3. Elbohy H, Thapa A, Poudel P, Adhikary N, Venkatesan S, Qiao Q. Vanadium oxide as new charge recombination blocking layer for high efficiency dye-sensitized solar cells. *Nano Energy* 2015, **13:** 368-375.

4. Thapa A, Zai J, Elbohy H, Poudel P, Adhikari N, Qian X*, et al.* TiO2 coated urchin-like SnO2 microspheres for efficient dye-sensitized solar cells. *Nano Res* 2014, **7**(8)**:** 1154-1163.

5. Gong J, Qiao H, Sigdel S, Elbohy H, Adhikari N, Zhou Z*, et al.* Characteristics of SnO2 nanofiber/TiO2 nanoparticle composite for dye-sensitized solar cells. *AIP Advances* 2015, **5**(6)**:** 067134.

6. Sigdel S, Elbohy H, Jiawei G, Adhikari N, Sumathy K, Hui Q*, et al.* Dye-Sensitized Solar Cells Based on Porous Hollow Tin Oxide Nanofibers. *Electron Devices, IEEE Transactions on* 2015, **62**(6)**:** 2027-2032.

7. Jianyuan Sun LZ, Ashishi Dubey, Swaminathan Venkatesan, Ting-Yu Lin, Logan Sanow, Yu-Chueh Hung, Qiquan Qiao, and Cheng Zhang. . Ring-protected small molecules for organic photovoltaics. *SPIE Meeting, August 25-29, 2013* 2013**:** 8830-8896.

8. Kumar M, Dubey A, Reza KM, Adhikari N, Qiao Q, Bommisetty V. Origin of photogenerated carrier recombination at the metal-active layer interface in polymer solar cells. *Phys Chem Chem Phys* 2015, **17**(41)**:** 27690-27697.

9. Mitul AF, Mohammad L, Vaagensmith B, Dubey A, Khatiwada D, Qiao Q. Optimization of Interconnecting Layers for Double- and Triple-Junction Polymer Solar Cells. *Photovoltaics, IEEE Journal of* 2015, **5**(6)**:** 1674-1679.

10. Mohammad L, Farzan Mitul A, Sigdel S, Dubey A, Khatiwada D, Adhikari N*, et al.* Interface Modification of Inverted Structure PSBTBT:PC70BM Solar Cells for Improved Performance. *Photovoltaics, IEEE Journal of* 2015, **5**(6)**:** 1659-1664.

11. Mohammad L, Mitul A, Qi W, Venkatesan S, Khatiwada D, Dubey A*, et al.* Influence of Nanoscale Morphology on Performance of Inverted Structure Metallated Conjugated Polymer Solar Cells. *Electron Devices, IEEE Transactions on* 2015, **62**(9)**:** 3029-3033.

12. Khatiwada D, Venkatesan S, Chen Q, Chen J, Adhikari N, Dubey A*, et al.* Improved performance by morphology control via fullerenes in PBDT-TBT-alkoBT based organic solar cells. *Journal of Materials Chemistry A* 2015, **3**(29)**:** 15307-15313.

13. Adhikari N, Khatiwada D, Dubey A, Qiao Q. Device and morphological engineering of organic solar cells for enhanced charge transport and photovoltaic performance. *Journal of Photonics for Energy* 2015, **5**(1)**:** 057207-057207.

14. Khatiwada D, Venkatesan S, Jihua C, Qiliang C, Adhikari N, Dubey A*, et al.* Morphological Evolution and Its Impacts on Performance of Polymer Solar Cells. *Electron Devices, IEEE Transactions on* 2015, **62**(4)**:** 1284-1290.

15. Venkatesan S, Chen J, Ngo EC, Dubey A, Khatiwada D, Zhang C*, et al.* Critical role of domain crystallinity, domain purity and domain interface sharpness for reduced bimolecular recombination in polymer solar cells. *Nano Energy* 2015, **12**(0)**:** 457-467.

16. Mitul AF, Mohammad L, Venkatesan S, Adhikari N, Sigdel S, Wang Q*, et al.* Low temperature efficient interconnecting layer for tandem polymer solar cells. *Nano Energy* 2015, **11**(0)**:** 56-63.

17. Venkatesan S, Ngo EC, Chen Q, Dubey A, Mohammad L, Adhikari N*, et al.* Benzothiadiazole-based polymer for single and double junction solar cells with high open circuit voltage. *Nanoscale* 2014, **6**(12)**:** 7093-7100.

18. Venkatesan S, Chen Q, Ngo EC, Adhikari N, Nelson K, Dubey A*, et al.* Polymer Solar Cells Processed Using Anisole as a Relatively Nontoxic Solvent. *Energy Technology* 2014, **2**(3)**:** 269-274.

19. Venkatesan S, Adhikari N, Chen J, Ngo EC, Dubey A, Galipeau DW*, et al.* Interplay of nanoscale domain purity and size on charge transport and recombination dynamics in polymer solar cells. *Nanoscale* 2014, **6**(2)**:** 1011-1019.

20. Dubey A, Qiao Q. Polymer-Inorganic Hybrid Solar Cells. *Polymers for Energy Storage and Conversion*. John Wiley & Sons, Inc., 2013, pp 163-197.

21. Dubey A, Zai J, Qian X, Qiao Q. Metal Oxide Nanocrystals and Their Properties for Application in Solar Cells. In: Bhushan B, Luo D, Schricker SR, Sigmund W, Zauscher S (eds). *Handbook of Nanomaterials Properties*. Springer Berlin Heidelberg, 2014, pp 671-707.

22. Dubey A, Saini P, Qiao Q. Conjugated Polymers-Based Blends, Composites and Copolymers for Photovoltaics. *Fundamentals of Conjugated Polymer Blends, Copolymers and Composites*. John Wiley & Sons, Inc., 2015, pp 281-338.

23. Adhikary P, Venkatesan S, Adhikari N, Maharjan PP, Adebanjo O, Chen J*, et al.* Enhanced charge transport and photovoltaic performance of PBDTTT-C-T/PC70BM solar cells via UV-ozone treatment. *Nanoscale* 2013, **5**(20)**:** 10007-10013.

24. Gong J, Darling SB, You F. Perovskite photovoltaics: life-cycle assessment of energy and environmental impacts. *Energy Environ Sci* 2015, **8**(7)**:** 1953-1968.

25. Khatiwada D, Venkatesan S, Adhikari N, Dubey A, Mitul AF, Mohammad L*, et al.* Efficient Perovskite Solar Cells by Temperature Control in Single and Mixed Halide Precursor Solutions and Films. *J Phys Chem C* 2015.

26. Wu C-G, Chiang C-H, Tseng Z-L, Nazeeruddin MK, Hagfeldt A, Gratzel M. High efficiency stable inverted perovskite solar cells without current hysteresis. *Energy Environ Sci* 2015.

27. Ahn N, Son D-Y, Jang I-H, Kang SM, Choi M, Park N-G. Highly Reproducible Perovskite Solar Cells with Average Efficiency of 18.3% and Best Efficiency of 19.7% Fabricated via Lewis Base Adduct of Lead(II) Iodide. *J Am Chem Soc* 2015, **137**(27)**:** 8696-8699.

28. Dubey A, Adhikari N, Venkatesan S, Gu S, Khatiwada D, Wang Q*, et al.* Solution processed pristine PDPP3T polymer as hole transport layer for efficient perovskite solar cells with slower degradation. *Sol Energy Mater Sol Cells*.

29. Jeng J-Y, Chiang Y-F, Lee M-H, Peng S-R, Guo T-F, Chen P*, et al.* CH3NH3PbI3 Perovskite/Fullerene Planar-Heterojunction Hybrid Solar Cells. *Adv Mater* 2013, **25**(27)**:** 3727-3732.

30. Rong Y, Tang Z, Zhao Y, Zhong X, Venkatesan S, Graham H*, et al.* Solvent engineering towards controlled grain growth in perovskite planar heterojunction solar cells. *Nanoscale* 2015, **7**(24)**:** 10595-10599.

31. Jeon NJ, Noh JH, Kim YC, Yang WS, Ryu S, Seok SI. Solvent engineering for high-performance inorganic–organic hybrid perovskite solar cells. *Nat Mater* 2014, **13**(9)**:** 897-903.

32. Yeo J-S, Kang R, Lee S, Jeon Y-J, Myoung N, Lee C-L*, et al.* Highly efficient and stable planar perovskite solar cells with reduced graphene oxide nanosheets as electrode interlayer. *Nano Energy* 2015, **12:** 96-104.

33. Burschka J, Pellet N, Moon S-J, Humphry-Baker R, Gao P, Nazeeruddin MK*, et al.* Sequential deposition as a route to high-performance perovskite-sensitized solar cells. *Nature* 2013, **499**(7458)**:** 316-319.

34. Xiao Z, Bi C, Shao Y, Dong Q, Wang Q, Yuan Y*, et al.* Efficient, high yield perovskite photovoltaic devices grown by interdiffusion of solution-processed precursor stacking layers. *Energy Environ Sci* 2014, **7**(8)**:** 2619-2623.

35. Chen Q, Zhou H, Hong Z, Luo S, Duan H-S, Wang H-H*, et al.* Planar Heterojunction Perovskite Solar Cells via Vapor-Assisted Solution Process. *J Am Chem Soc* 2014, **136**(2)**:** 622-625.

36. Liu M, Johnston MB, Snaith HJ. Efficient planar heterojunction perovskite solar cells by vapour deposition. *Nature* 2013, **501**(7467)**:** 395-398.

37. Barrows AT, Pearson AJ, Kwak CK, Dunbar ADF, Buckley AR, Lidzey DG. Efficient planar heterojunction mixed-halide perovskite solar cells deposited via spray-deposition. *Energy Environ Sci* 2014, **7**(9)**:** 2944-2950.

38. Yang WS, Noh JH, Jeon NJ, Kim YC, Ryu S, Seo J*, et al.* High-performance photovoltaic perovskite layers fabricated through intramolecular exchange. *Science* 2015, **348**(6240)**:** 1234-1237.

39. Yang B, Dyck O, Poplawsky J, Keum J, Puretzky A, Das S*, et al.* Perovskite Solar Cells with Near 100% Internal Quantum Efficiency Based on Large Single Crystalline Grains and Vertical Bulk Heterojunctions. *J Am Chem Soc* 2015, **137**(29)**:** 9210-9213.

40. Chen Y, Zhao Y, Liang Z. Non-Thermal Annealing Fabrication of Efficient Planar Perovskite Solar Cells with Inclusion of NH4Cl. *Chem Mater* 2015, **27**(5)**:** 1448-1451.

41. Zhou Y, Yang M, Wu W, Vasiliev AL, Zhu K, Padture NP. Room-temperature crystallization of hybrid-perovskite thin films via solvent-solvent extraction for high-performance solar cells. *Journal of Materials Chemistry A* 2015, **3**(15)**:** 8178-8184.

42. Zhang W, Saliba M, Moore DT, Pathak SK, Hörantner MT, Stergiopoulos T*, et al.* Ultrasmooth organic–inorganic perovskite thin-film formation and crystallization for efficient planar heterojunction solar cells. *Nat Commun* 2015, **6**.

43. Wong AB, Lai M, Eaton SW, Yu Y, Lin E, Dou L*, et al.* Growth and Anion Exchange Conversion of CH3NH3PbX3 Nanorod Arrays for Light-Emitting Diodes. *Nano Lett* 2015, **15**(8)**:** 5519-5524.

44. Sun K, Chang J, Isikgor FH, Li P, Ouyang J. Efficiency enhancement of planar perovskite solar cells by adding zwitterion/LiF double interlayers for electron collection. *Nanoscale* 2015, **7**(3)**:** 896-900.

45. Stoumpos CC, Malliakas CD, Kanatzidis MG. Semiconducting Tin and Lead Iodide Perovskites with Organic Cations: Phase Transitions, High Mobilities, and Near-Infrared Photoluminescent Properties. *Inorg Chem* 2013, **52**(15)**:** 9019-9038.

46. Hao F, Stoumpos CC, Liu Z, Chang RPH, Kanatzidis MG. Controllable Perovskite Crystallization at a Gas–Solid Interface for Hole Conductor-Free Solar Cells with Steady Power Conversion Efficiency over 10%. *J Am Chem Soc* 2014, **136**(46)**:** 16411-16419.

47. Dong Q, Yuan Y, Shao Y, Fang Y, Wang Q, Huang J. Abnormal crystal growth in CH3NH3PbI3-xClx using a multi-cycle solution coating process. *Energy Environ Sci* 2015, **8**(8)**:** 2464-2470.

48. Christians JA, Miranda Herrera PA, Kamat PV. Transformation of the Excited State and Photovoltaic Efficiency of CH3NH3PbI3 Perovskite upon Controlled Exposure to Humidified Air. *J Am Chem Soc* 2015, **137**(4)**:** 1530-1538.

49. Yang J, Siempelkamp BD, Liu D, Kelly TL. Investigation of CH3NH3PbI3 Degradation Rates and Mechanisms in Controlled Humidity Environments Using in Situ Techniques. *ACS Nano* 2015, **9**(2)**:** 1955-1963.

50. Imler GH, Li X, Xu B, Dobereiner GE, Dai H-L, Rao Y*, et al.* Solid state transformation of the crystalline monohydrate (CH3NH3)PbI3(H2O) to the (CH3NH3)PbI3 perovskite. *Chem Commun* 2015, **51**(56)**:** 11290-11292.

51. Leguy AMA, Hu Y, Campoy-Quiles M, Alonso MI, Weber OJ, Azarhoosh P*, et al.* Reversible Hydration of CH3NH3PbI3 in Films, Single Crystals, and Solar Cells. *Chem Mater* 2015, **27**(9)**:** 3397-3407.

52. Bass KK, McAnally RE, Zhou S, Djurovich PI, Thompson ME, Melot BC. Influence of moisture on the preparation, crystal structure, and photophysical properties of organohalide perovskites. *Chem Commun* 2014, **50**(99)**:** 15819-15822.

53. Vincent BR, Robertson KN, Cameron TS, Knop O. Alkylammonium lead halides. Part 1. Isolated PbI64− ions in (CH3NH3)4PbI6•2H2O. *Can J Chem* 1987, **65**(5)**:** 1042-1046.

54. Cui P, Fu P, Wei D, Li M, Song D, Yue X*, et al.* Reduced surface defects of organometallic perovskite by thermal annealing for highly efficient perovskite solar cells. *RSC Advances* 2015, **5**(92)**:** 75622-75629.

55. Lian J, Wang Q, Yuan Y, Shao Y, Huang J. Organic solvent vapor sensitive methylammonium lead trihalide film formation for efficient hybrid perovskite solar cells. *Journal of Materials Chemistry A* 2015, **3**(17)**:** 9146-9151.